DOMINIK BUKSA
PAWEŁ MADEJSKI
MICHAŁ KARCH

Rapid prototyping of water nozzles using CFD modeling and 3D printing results

In recent years, there has been greater interest in rapid prototyping methods employed in various industries. Prototypes are increasingly often made using 3D printing technology, which is mainly due to the relatively low costs of developing and producing such a structure and the short time needed for their physical production. The work presents the possibility of using rapid prototyping techniques, such as water propulsion nozzles. They are mainly used in the energy industry, e.g. for the production of water mist in jets or condensers. Such nozzles enable the formation of a stream, and its range and efficiency depend on the design requirements. CFD (computational fluid dynamics) tools and 3D printing will be used to assess the nozzle's effectiveness. A 3D printer based on FDM technology was used to produce nozzle prototypes. The CFD results were verified with experiment. Analyzes for four different nozzle shapes are presented and the discrepancies between the results of the initial experimental and numerical analyses are explained. To indicate the imperfections resulting from 3D printing, a 3D scanner was used to show the internal cross-section of the nozzle. The research conducted indicates the significant potential of 3D printing in rapid prototyping and its effectiveness in creating functional models for various engineering applications.

Key words: *CFD, rapid prototyping, 3D printing, water nozzles*

1. INTRODUCTION

Rapid prototyping is a group of techniques used to quickly create a three-dimensional scale model of a specific product or mechanical part [1]. It includes five stages [2]:

1. Creating a project: a 3D model of the object is created using CAD software.
2. Data preparation: processing the CAD model into an appropriate format, depending on the selected technology.
3. Device configuration: calibration, preparation, and ensuring of appropriate material used to build the facility.
4. Prototype construction: constructing a product by a machine in a specific way, e.g. layer by layer.
5. Post-processing: Prototypes often require post-processing to obtain the desired finish or mechanical properties. This process includes surface finishing by grinding, painting, or assembly.

In recent years, there has been an increasing interest in rapid prototyping methods which are employed in various areas, e.g. in medicine, where they are used for reconstruction and implantation purposes. The main techniques involving rapid prototyping are: Stereo-Lithography Apparatus (SLA), Selective Laser Sintering (SLS), Fused Deposition Modelling (FDM). Prototypes are increasingly made using 3D printing technology, which is mainly related to the relatively low cost of developing such a structure and the speed of the process [3]. Additionally, these techniques enable engineers to quickly pre-verify the product being developed. Therefore, it is possible to test more variants within a given time frame [4].

In industrial applications, rapid prototyping methods are often combined with numerical simulation. Considerable development can be observed, especially in the design processes of new aircraft where CFD models are considered the key to success. The article [5] examined prototypes of the Generic Future Fighter

aircraft. A CFD model was developed, using which the authors examined various angles of attack and slip angles for various variants of aircraft wings. The use of 3D printing made it possible to print parts used to assemble the wind tunnel and the aircraft object. The numerical simulation results were confirmed by wind tunnel tests for various variants. This was important because the project was based on an actual scale-built GFF aircraft that is radio-controlled. The use of rapid prototyping, 3D printing and CFD enabled the creation of aircraft wings that are more effective and would be installed on this model in reality. It is estimated that the implementation of the entire project, including conceptual, simulation, and documentation, takes from 6 to 12 months, including real flight tests. 3D printing is part of the validation process supported by CFD. Often, good visualization of numerical calculations involves complex 3D shapes that can be difficult to recognize on 2D displays. An alternative approach is the 3D printing method, which prints objects representing the simulation results, e.g. temperature distributions on the walls inside the structure [6].

In the article, attention is focused on water nozzles which are used in many industries and households. They are components of complex, specialized devices as well as everyday appliances. The construction of nozzles and the processes for which they are used depend on their purpose. Most often they are used in processes in which it is necessary to properly direct and distribute the fluid (washing, descaling, spraying, cooling systems) [7]. In the power industry, they are used in water turbines (rotor speed control) [8], firefighting systems (as a water mist) [9], for spray cooling, quenching [10] and also in many other solutions. It is indicated that nozzles for the energy sector should provide ease of use, simple installation and maintenance. Such nozzles are also used in renewable energy sources, making them particularly interesting. In wind turbines they serve as a technique for de-icing the blades in winter, and in photovoltaics they provide an evenly distributed water jet that removes dirt without damaging the panels. Modern solutions for energy storage systems require strict control of humidity levels when using lithium materials. For this reason, water jets are used as a spray that produces air atomized droplets for better humidity control [11].

The article [12] describes the use of water nozzles in dust removal devices, e.g. to neutralize the explosive properties of mixtures in contact with air. The nozzles spray water, thanks to which solid particles (dust) are absorbed inside the water drops. The efficiency of the water nozzle depends on the energy contained in the outflowing water drops, resulting from the pressure generated by the pump supplying water to the nozzle. Therefore, vortex nozzles are increasingly used and the rotational movement of the rotor supplies the drops with kinetic energy.

The research in this article concerned the comparison of nozzle efficiency. The experiment examined the relationship between the nozzle volume flow and the pressure generated at its inlet.

2. NUMERICAL ANALYSIS

2.1. Geometry

For the nozzles presented below (Figs. 1–4), the same key dimensions have been maintained, which are marked in Figure 1. These nozzles differ in shape, which may have a significant impact on the way the water spreads and its speed. The shape and structure of the nozzles can affect whether the water stream will be more concentrated or dispersed, as well as its range.
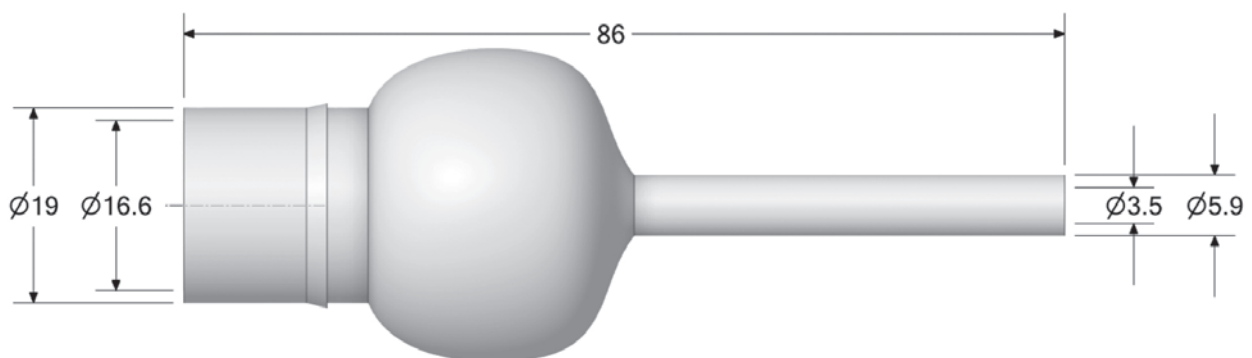

Fig. 1. Nozzle 1

Fig. 2. Nozzle 2

Fig. 3. Nozzle 3

Fig. 4. Nozzle 4

2.2. Discretization of the computational domain

The domain was discretized using Ansys Fluent Meshing software. A Poly-Hexcore Mosaic mesh was created. This technology connects any types of elements and is described in more detail in [13]. The fundamental advantage of using such shapes is reducing the number of mesh elements – generally by 20% to 50%, which speeds up calculations by an average of 10–50% [14]. The mesh construction process is different when using different turbulence models because each model has its own limitations and requirements. In the current model, inflation layers were used at the fluid-solid boundaries to keep the y+ value less than 2. This practice is recommended for the $k - \varepsilon$ realizable turbulence model using an advanced wall function [15].
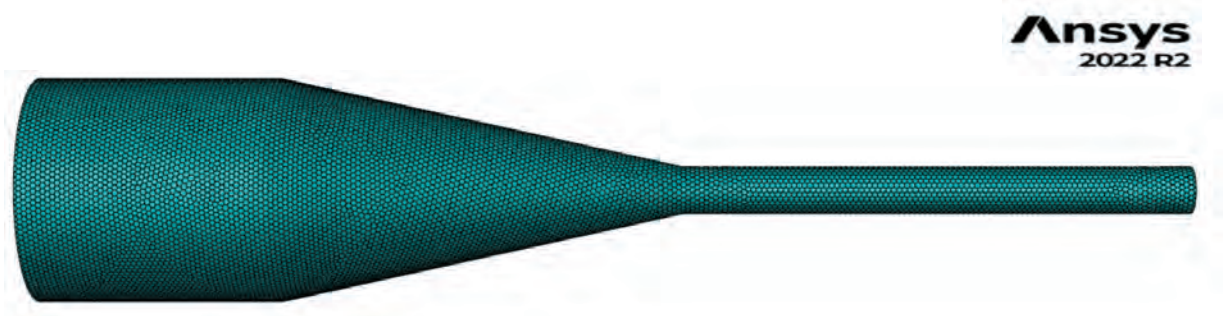

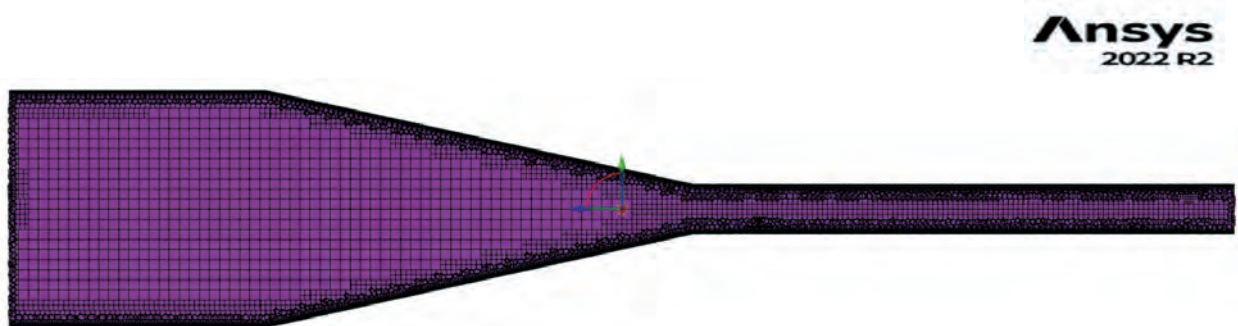*Fig. 5. Surface mesh of the nozzle*

Fig. 6. Volume mesh in the longitudinal section of the nozzle

A properly constructed mesh required the use of 12 inflation layers with an increase factor of 0.25. The height of the first cell was set to 0.0044 mm. The minimum length of a single element was 0.04 mm, while the maximum was 0.70 mm.

As intended, it was possible to create a mesh suitable for the tested turbulence models. The maximum value of the y+ parameter was 1.51 and occurred at the site of stenosis. Narrowing the cross-section of

the geometry compelled changes in the size of the mesh elements and the modeling of a smooth transition in this place, therefore the y+ value is the largest there because the first cell moved away from the wall. This was necessary to be able to model a smooth transition between subsequent mesh elements. The increase in the y+ value is also influenced by the change in speed, which causes an increase in wall shear stress.
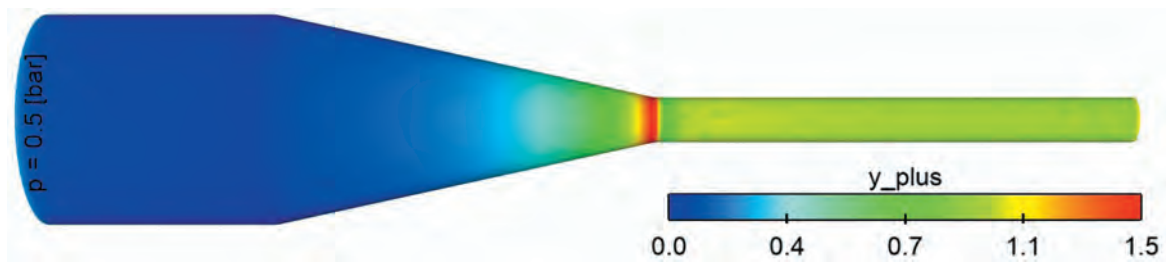

Fig. 7. Visualization of the y+ value for the constructed mesh

2.3. Mesh quality

Using three basic criteria that help determine mesh quality: skewness, orthogonality, and aspect ratio, the mesh was optimized to meet the recommendations requested by the researchers. The average values of these parameters for the analyzed geometry are presented in Table 1.

According to the user manual [15], satisfactory optimized parameter values were obtained. In the generated mesh, very small differences were found between the shape of an arbitrary cell and an equilateral cell.

The recommended condition that the maximum value of skewness should not exceed 0.95 was also met [17].

CFD solvers are most efficient for meshes that have a high orthogonality factor [18]. The values obtained allow us to state that the quality of the created elements is satisfactory.

The shape factor reached its maximum value for elements located in the boundary layer. If this value was significantly higher, it could affect the convergence of the solution, or the results obtained. The presented values and mesh tests indicate that the effect is not observable for the selected mesh.

Table 1

Quality parameters of the numerical mesh

Value	Skewness	Orthogonality	Aspect ratio
Minimum	0.00	0.48	1.00
Average	0.02	0.98	25.51
Maximum	0.51	1.00	126.67

2.4. Independence of the solution

Before selecting the final mesh used in the numerical analysis, the dependence of the obtained results on the number of its elements was examined. A constant boundary layer was previously established, in which $y+_{max} = 1.51$, $y+_{average} = 0.32$, so that only the number of elements related to their size and not the boundary layer changes. The study was carried out by ana-

lyzing the water mass flow rate at the nozzle outlet cross-section, because it is of fundamental importance in the current paper.

It transpired that as the number of mesh elements increases, the value of the water volume flow rate at the outlet cross-section also increases. The summation error can significantly impact the results, which is why the process of validating numerical simulations is so important. No significant differenc-

es were found when comparing a mesh containing 282 096 or more elements. Therefore, taking into account the computational cost, this mesh was selected as it will allow calculation times to be sped up while maintaining the same precision by saving workstation resources.
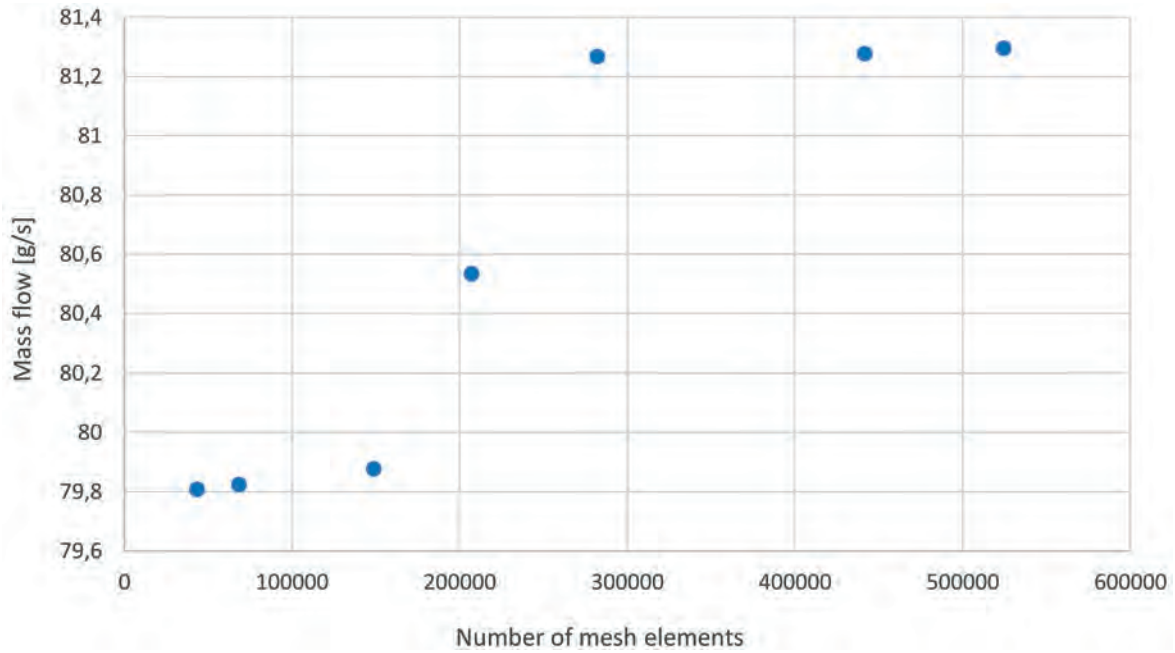

Fig. 8. Dependence of the volume flow rate at the nozzle outlet on the number of grid elements

2.5. Turbulence model, boundary conditions and numerical settings

Since the purpose of the simulation is to mainly study the nozzle's performance, and the model does not assume the use of an energy equation or multiphase model, the most universal turbulence model was used, that is, the hybrid $k - \omega$ SST model. This model is described by equations (1) and (2).

Turbulence kinetic energy k is described by the following equation:

$$\frac{\partial}{\partial t}(\rho k) + \frac{\partial}{\partial x_i}(\rho k u_i) =$$

$$= \frac{\partial}{\partial x_j}\left(F_k \frac{\partial k}{\partial x_j}\right) + G_k - Y_k + S_k + G_b \tag{1}$$

The specific dissipation rate ω is given as:

$$\frac{\partial}{\partial t}(\rho \omega) + \frac{\partial}{\partial x_i}(\rho \omega u_i) =$$

$$= \frac{\partial}{\partial x_j}\left(F_w \frac{\partial \omega}{\partial x_j}\right) + G_w - Y_w + S_w + G_{wb} \tag{2}$$

where:

t – time [s],
k – turbulence kinetic energy [J/kg],
x – spatial variable [m],
ρ – density [kg/m^3],
u – velocity [m/s],
F_k, F_w – terms modeling the effective diffusivity for k and ω [m^2/s],
G_k – generation of turbulence kinetic energy due to velocity gradients [J/(sm^3)],
Y_k, Y_w – dissipation k and ω due to turbulence [m^2/s^3],
S_k, S_w – user-defined source terms [J/(sm^3)],
G_k, Y_{wb} – generation of turbulence kinetic energy due to the buoyancy force [J/(sm^3)].

Available methods of modeling the terms contained in equations (1) and (2) are presented in the Ansys Fluent user manual [19].

The following **boundary conditions** were assumed for the model:
- Inlet: condition based on gauge pressure. The following values were tested: 0.5, 1, 2, 3, 4, 5, 6, 7, 8 bar.
- Outlet: pressure condition with outlet overpressure reference value 0 Pa.
- Walls: it is assumed that the walls are perfectly insulated.

For the purposes of the current simulation, the following was assumed:

- incompressible flow, so a pressure-based solver was used;
- steady-state, with gravity turned off;
- coupled solution scheme;
- discretization of conservation equations with second-order schemes;
- when controlling the stability of the solution, the pseudo-time step was disabled and an approach based on the Courant number was used. It is indicated that full stability reaches the maximum CFL in the range of 5–100 [20], a value of 10 was used in the current simulation.

2.6. Results of numerical analysis

Figure 9 shows a comparison of the results obtained during the numerical analysis for the four tested nozzles. According to what will be verified in reality, the attention is focused on the mass flow at the outlet cross-section from the nozzle.

It turns out that nozzle number 3 is the most effective since it produced the highest water mass flow with the same inlet pressure values. The greatest flow resistance was experienced by geometry 2, in which the medium flow rate was the lowest. As the inlet pressure increases, the differences between the analyzed nozzle variants become larger. This situation is clearly observable when comparing the pairs of variants: 1 with 3 and 2 with 4. At the inlet pressure of 0.5 bar, the mass flows for the pairs in question are almost the same. Subsequently, each modification that involves exerting greater pressure at the inlet to the system causes the flow in one of the nozzles to deviate more and more from the other.

In the next steps, numerical analysis will be performed for variant 3 of the nozzle, the results of which turned out to be the most promising. The presented visualization will concern cases in which the inlet pressure was 0.5 bar and 8 bar. If there are no differences between the variants that are interesting from the point of view of the current work, only one case will be presented.

Because the presented geometry is not complex and the working medium is water, which has a high density, no intense reverse vortices that could affect the shape of the flow were found (Figs. 10 and 11).

The constructed geometry results in an almost perfect arrangement of velocity vectors, which are visible in greater numbers mainly near the walls. Water molecules slide on the walls because the change in cross-section is not sudden but gradual. Forcing the pressure at the inlet to be as much as 16 times higher resulted in a maximum of 4 times greater increase in the flow speed.
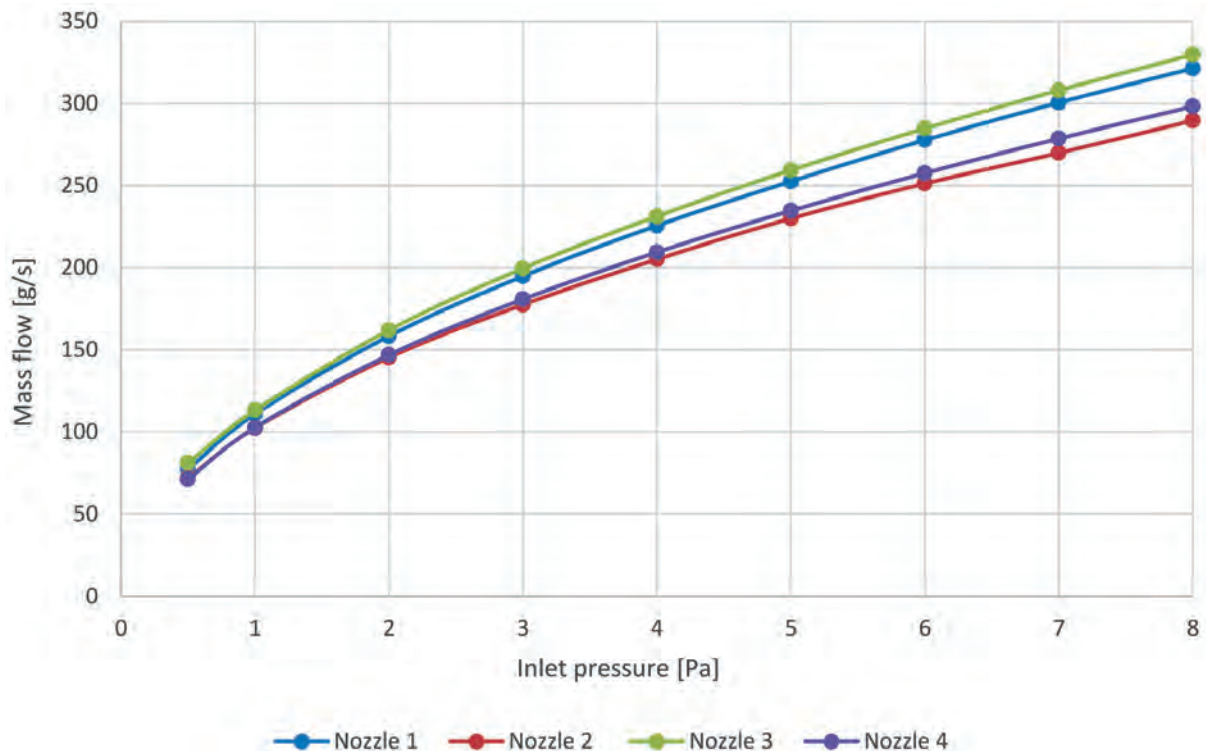

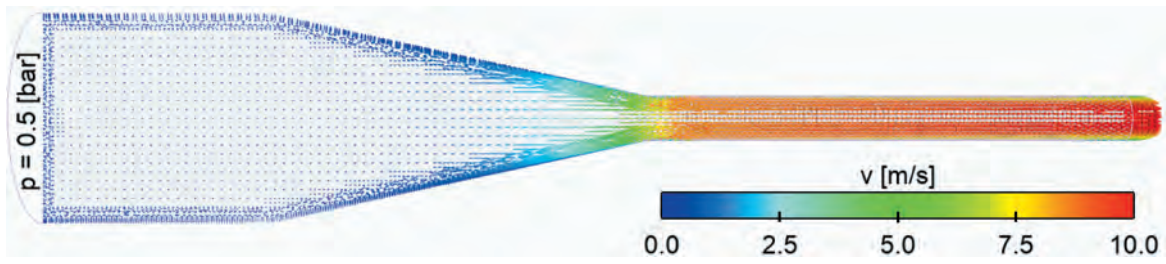*Fig. 9. Comparison of CFD results for the analyzed nozzle shapes*

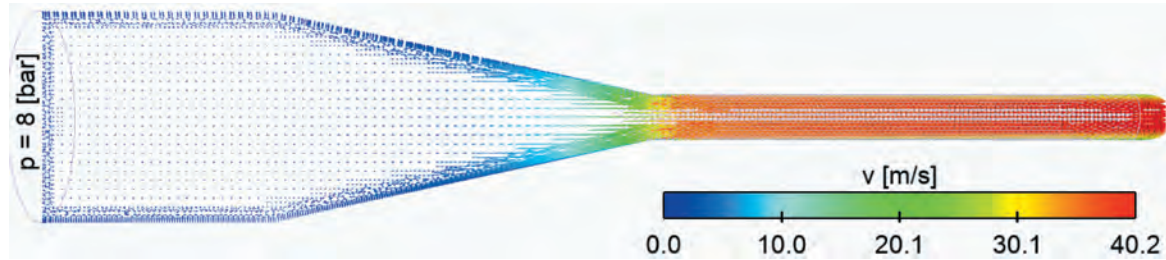*Fig. 10. Velocity vectors for the longitudinal section of the nozzle, p = 0.5 bar*

Fig. 11. Velocity vectors for the longitudinal section of the nozzle, p = 8 bar

Note: The increased number of vectors at the walls is only related to the structure of the mesh. This area has a boundary layer, so the elements are more densely packed.

To confirm the conclusions drawn when discussing the velocity vectors for the longitudinal section, streamlines drawn throughout the nozzle volume were also analyzed (Fig. 12). It was found that the stream is very well formed, and the appropriately selected, gentle narrowing and axial symmetry of the nozzle eliminate the occurrence of any recirculation. This is a desirable phenomenon because recirculation zones would slow the flow of fluid through the outlet channel. Apart from the differences in the speed values, which were discussed in the analysis of Figure 13, there are no significant differences in the formation of the stream for an inlet pressure of 8 bar.

The intensification of the kinetic energy of turbulence mainly occurs in the outlet part of the nozzle which is responsible for straightening/forming the stream. This is certainly related to the sudden increase in fluid velocity that occurred in this place. The rapid narrowing of the cross-section caused chaotic movement of particles, which collided with each other and increased the resulting vortices and turbulence. At a pressure of 8 bar, the increase in the kinetic energy of turbulence is even more than 22 times greater.
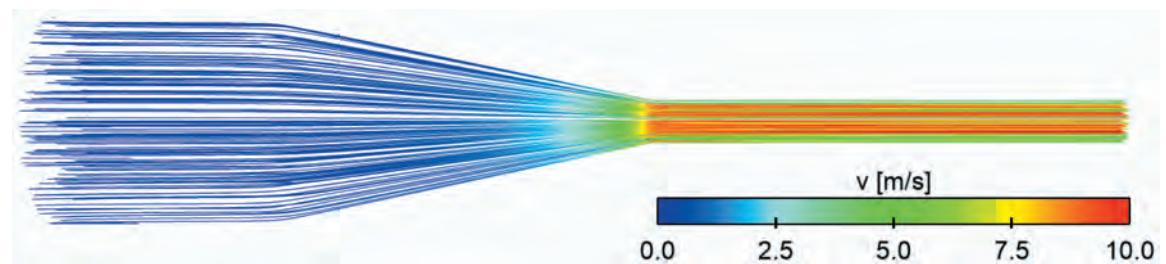

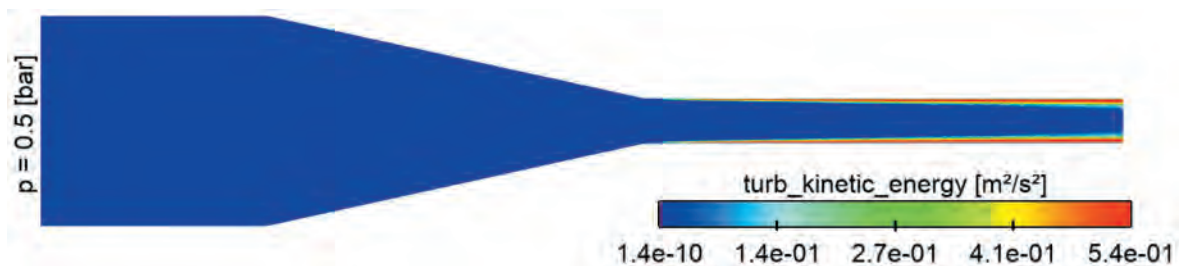*Fig. 12. Streamlines for the longitudinal section of the nozzle, p = 0.5 bar*

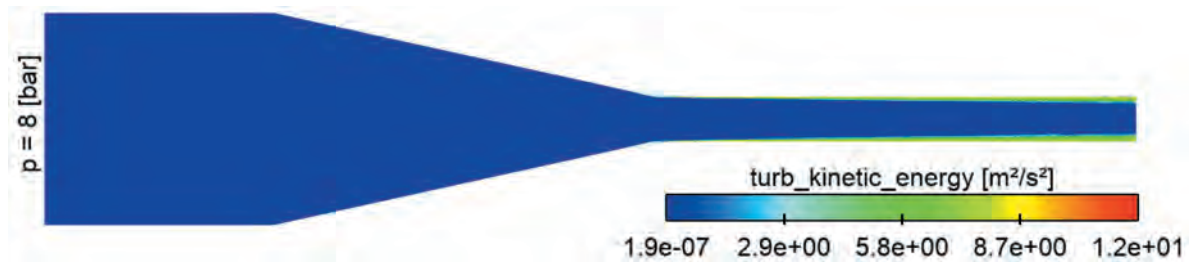*Fig. 13. Turbulence kinetic energy for the longitudinal section of the nozzle, p = 0.5 bar*

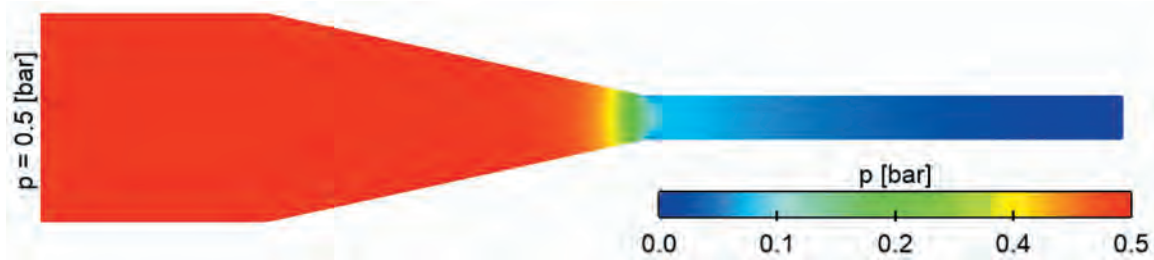*Fig. 14. Turbulence kinetic energy for the longitudinal section of the nozzle, p = 8 bar*

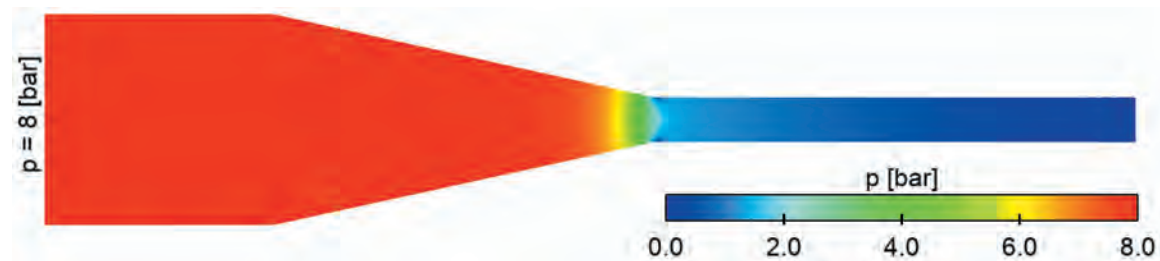*Fig. 15. Static pressure drop for the longitudinal section of the nozzle, p = 0.5 bar*

Fig. 16. Static pressure drop for the longitudinal section of the nozzle, p = 8 bar

Each narrowing of the flow cross-section, which resulted in an increase in velocity, also causes a decrease in static pressure. This process is strongly related to the compressibility of the fluid, which does not occur in this case. Therefore, the volume of fluid that flows through the initial cross-section is equal to the volume that flows through the constriction. The flowing water exerts less pressure on the nozzle walls because the stream direction is focused horizontally toward the outlet.

This phenomenon is consistent with the Bernoulli equation (1), which describes the behavior of the total energy density along the streamline. Bernoulli's equation in the form:

$$p + \frac{1}{2}\rho v^2 + \rho g h = \text{const} \tag{1}$$

indicates that the sum of static pressure $(1/2\rho v^2)$, dynamic pressure (p) and hydrostatic pressure (pgh) along a streamline is constant for an incompressible and inviscid fluid. Considering the equation as an ap-

proximation (neglecting viscous forces), as the flow cross section narrows, the flow velocity v increases (according to the continuity equation), which leads to an increase in dynamic pressure. Since the sum of the total energy density remains constant, an increase in dynamic pressure results in a decrease in static pressure.

The velocity field distribution (Fig. 17) is consistent with the distribution of pressure drop in the nozzle presented in Figure 16. Because the nozzle channel is simple (with no complicated elements), and complete symmetry, the velocity field is also symmetrical. Analyzing the cross-sections in terms of speed changes, it turns out that there are no significant differences. The fluid moves fastest at the center of symmetry, but the difference between the center and points near the wall does not exceed 12.5%.

In order to compare the differences in the results obtained for different variants, it was decided to also present a visualization for nozzle 1, whose mass flow results were most similar to the results of the nozzle previously discussed.

The analysis of the streamlines for nozzle 1 allowed for the identification of significant differences in the hydrodynamic nature of the flow. It turns out that significant reverse vortices occur already at an inlet pressure of 0.5 bar. Moreover, as the pressure increases to 8 bar, they become more and more intense. The stream slides along the wall and returns to the main flow. However, it should be noted that there are also areas where particles fall into the vortex and do not return to the main stream, the swirled stream blocks the main flow.

The velocity vectors confirm previous observations and additionally show that vortices are not only present in the extended part of the geometry but also in the main stream. What was found is the complete opposite of what was discussed in the analysis of nozzle 3 (Fig. 12). Because the flow has become complex and the vortices are chaotic, the flow is not symmetrical. This is manifested by the fact that when the flow cross-section changes, the particles hit the narrowed walls of the outlet channel unevenly. This may cause damage to the nozzle at this point, especially at high speeds.
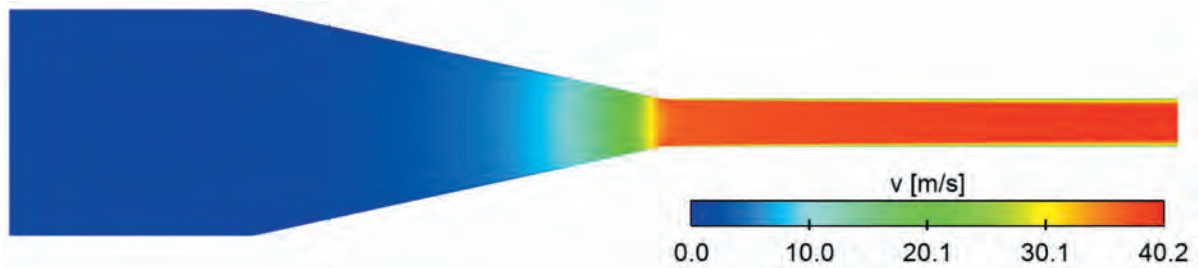

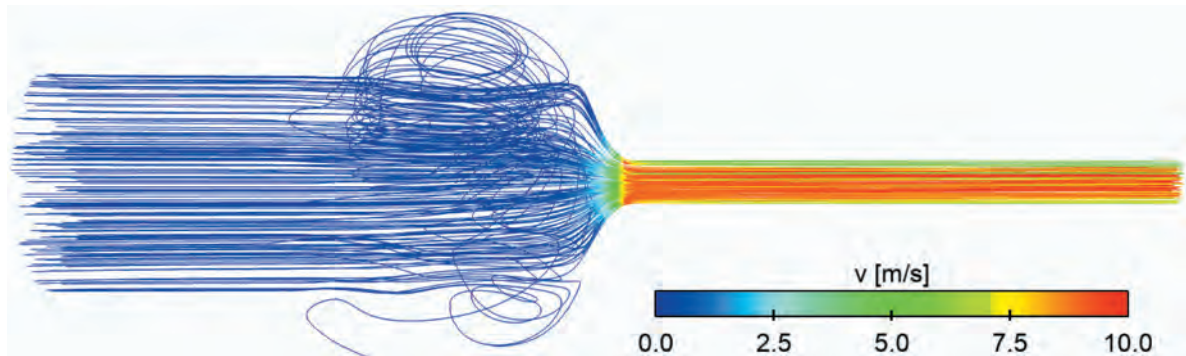Fig. 17. Distribution of the velocity field in the nozzle, p = 8 bar

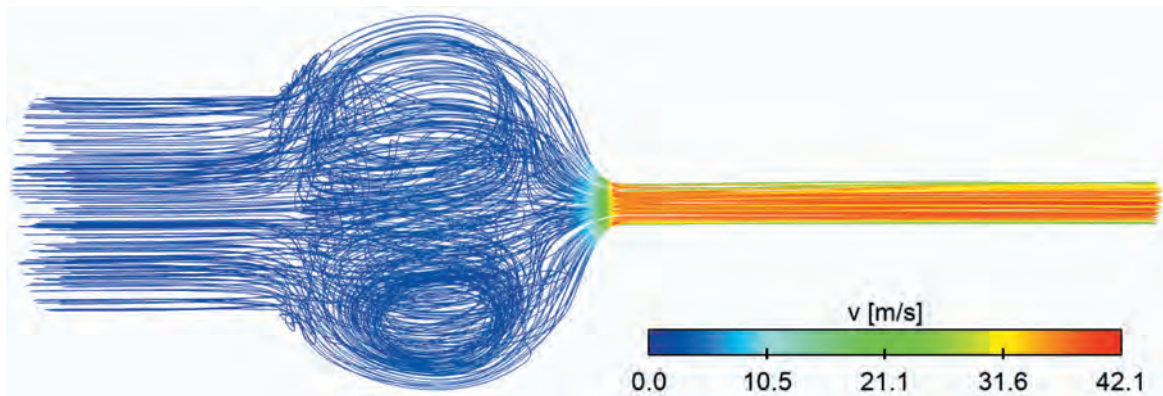Fig. 18. Streamlines for the longitudinal section of the nozzle, p = 0.5 bar

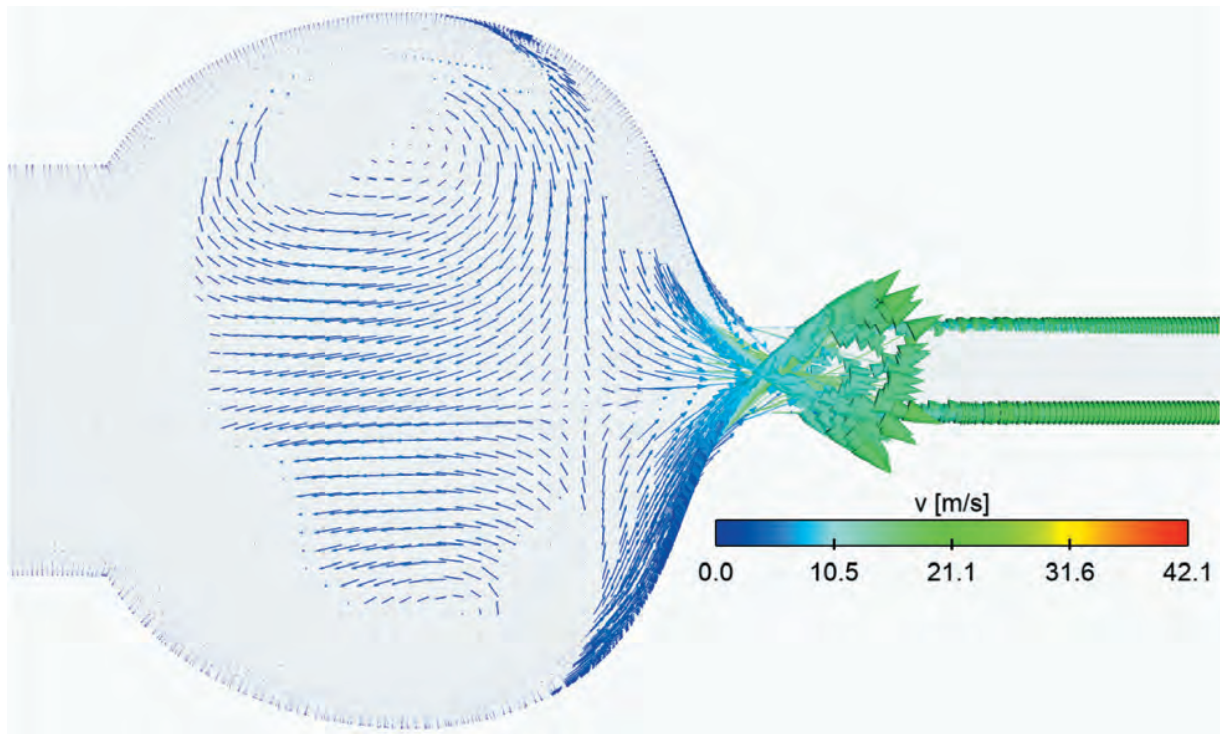Fig. 19. Streamlines for the longitudinal section of the nozzle, p = 8 bar

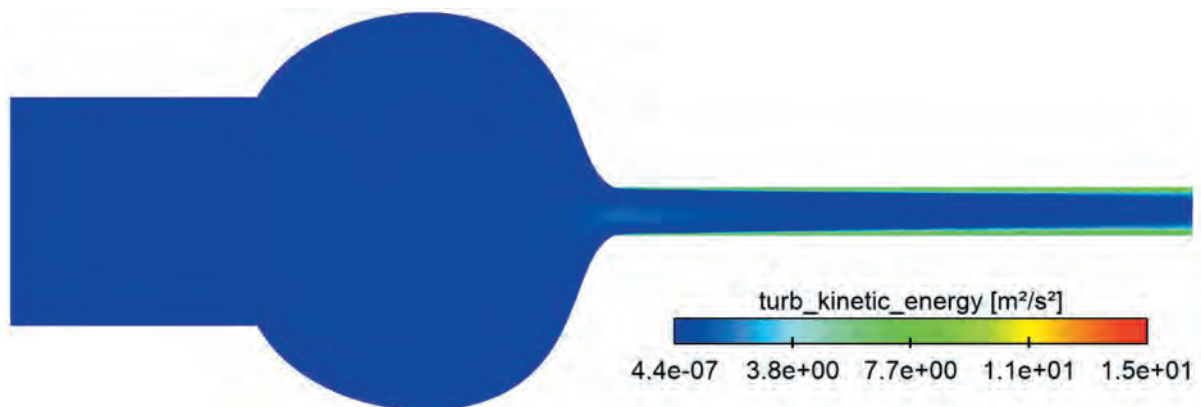*Fig. 20. Velocity vectors for the longitudinal section of the nozzle, p = 8 bar*

Fig. 21. Turbulence kinetic energy for the longitudinal section of the nozzle, p = 8 bar

The intensification of the kinetic energy of turbulence not only occurs in the outlet channel near the walls into which the water molecules hit, but also in the geometric center of the channel. This phenomenon was not observed in the visualizations regarding nozzle 3 (Fig. 14). Moreover, the analyzed nozzle is characterized by a maximum increase in turbulence kinetic energy by as much as 25% compared to variant 3, which is caused by its specific geometry.

The cross-section expansion did not result in significant changes in static pressure, which remained approximately constant. At the point where the cross-section changed in the outlet channel, there was a sudden pressure drop from 8 to 2.5 bar. Two blue zones are also visible, where negative pressure was found. This suggests the possibility of cavitation occurring in this place. Therefore, it was decided to analyze the distribution of the velocity field for this variant.

Analyzing the velocity field, it was found that it is not uniform and symmetrical. It turns out that in the cross-section, the velocity values change even several times (Fig. 23). Moreover, in the place where the negative pressure was found (Fig. 22), the stream detaches from the narrowing edge, which is caused by the high-speed value in this place (approx. 35 m/s) and the specific geometry in which the transition is not smoothly designed. Therefore, the fluid flow in this area is characterized by its complexity.
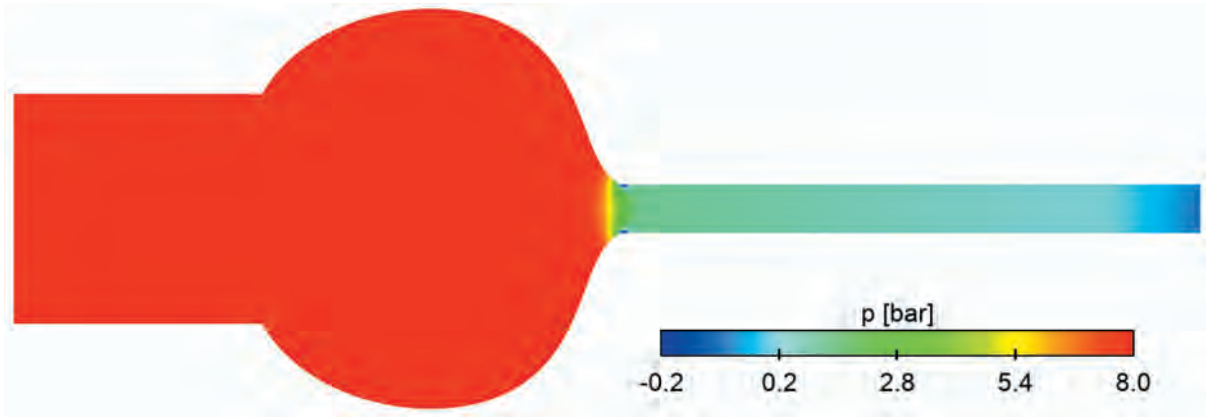
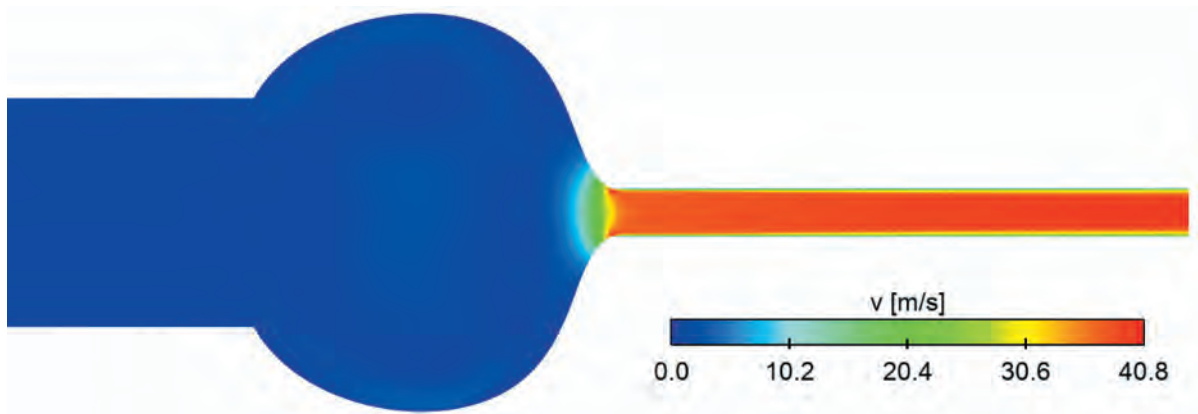*Fig. 22. Static pressure drop for the longitudinal section of the nozzle, p = 8 bar*

*Fig. 23. Distribution of the velocity field in the nozzle, p = 8 bar*

3. MODEL VERIFICATION

3.1. 3D printing

In order to verify the developed nozzle models in numerical analysis, it was decided to create their actual prototypes. Due to the availability of equipment, low costs, and short construction time, 3D print-ing technology was chosen to complete this task. An Original Prusa i3 3D printer, which uses FDM print-ing technology, was used. The process of creating three-dimensional objects involves melting and ap-plying thin layers of thermoplastic filament through a moving nozzle. The longitudinal section (Fig. 24) shows one of the selected nozzles so as to be able to see its deficiencies compared to the ideal model.
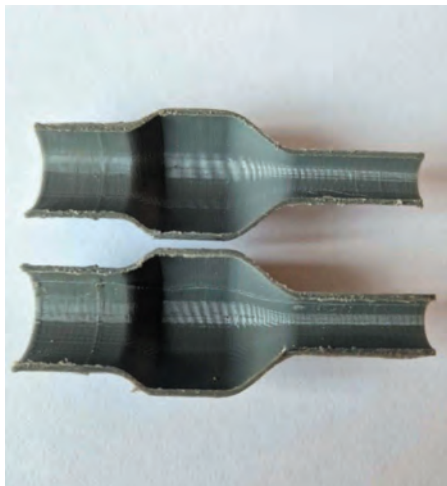
a)   *b)*

Fig. 24. Longitudinal section of the printed nozzle: a) photo; b) 3D scan

Nozzles printed using FDM technology are characterized by a layered structure that affects the roughness of the internal surfaces. This layering can lead to increased flow resistance and greater energy loss. Additionally, there may be minor discontinuities and inaccuracies resulting from the printer's limited precision and the filament's properties. These factors mean that the flow in the real nozzle may differ from the flow in the ideal CFD model, which should be taken into account in the analyzes and interpretation of the results.

3.2. Laboratory experiment

Using a simple measurement system consisting of a water pump, a water tank, a garden hose, and fittings, a preliminary verification of the obtained CFD simulation results for two nozzle variants was carried out.

1 – water tank
2 – support
3 – water pump
4 – hose (suction side)
5 – hose (water discharge side)
6 – control valve
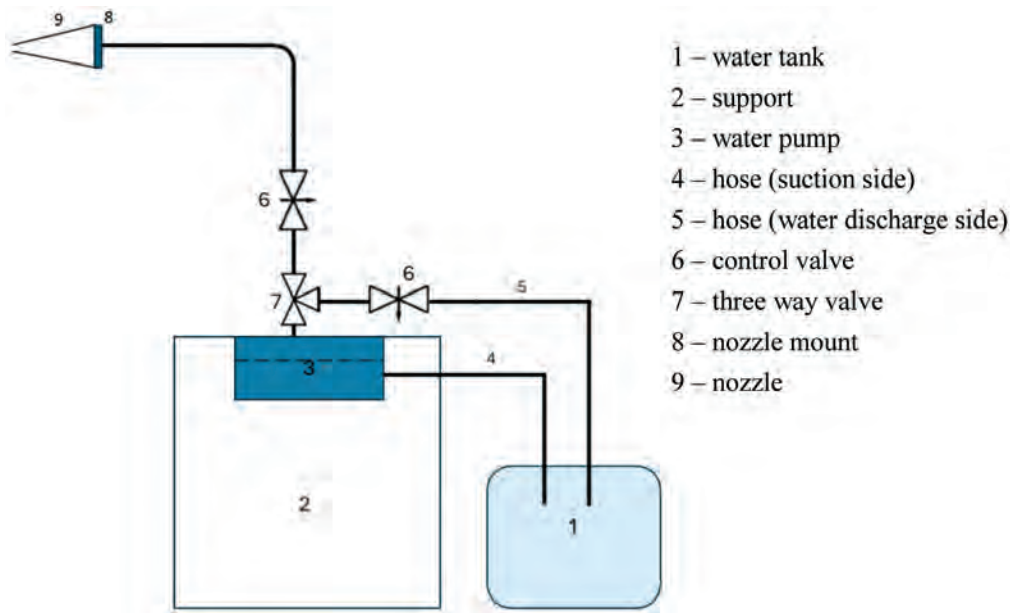7 – three way valve
8 – nozzle mount
9 – nozzle

Fig. 25. Scheme of the measuring station

Description of the experiment: The test involved filling a 15-liter tank with water at various pressures generated by the pump. Various variants of nozzles were mounted to the hose connected to the pump fittings. The pressure generated by the pump was measured using a manometer placed on the discharge line. The pump operating range was tested from 0.5 to 8 bar. The time needed for each nozzle to fill the tank was measured using a stopwatch, and then the water tank was placed on a laboratory scale. Taking into account the filling time and the mass of water in the tank, the water mass flow g/s was calculated and compared to the results obtained from CFD. The mass flow rates of water obtained in the conducted experiment are shown in Figure 26.

The experiment shows, in accordance with the results of the numerical analysis, that nozzle 3 is more effective in comparison to nozzle No. 1. The differences found in the mass flow for both nozzles are in the range of 2.5 to 26.8%. The nature of the increase in mass flow with increasing pressure for nozzle 1 is more intense.

Comparing the results of the CFD experiment (Fig. 27) for nozzle 1, differences in the mass flow

value were found ranging from 13.1 to 32.3%, which translated into differences from 10.1 to 77.1 g/s. It was observed that approximately the nature of the mass flow function from the inlet pressure for both the experiment and CFD is similar.

Analyzing the comparative results for nozzle 3 (Fig. 28), also found significant discrepancies. Measurements made for the lowest values of inlet pressures, i.e. 0.5, 1 bar, are highly consistent (the maximum relative error was 5.5%). However, as the inlet pressure increases, the measurements are less and less consistent with the results of the numerical analysis, increasing the maximum relative error to as much as 20.8%. It is assumed that this may be due to the fact that the pressure was controlled using a manometer, and therefore the pulsations generated by the pump made it difficult to read the values accurately. The higher the pressure, the more difficult it was to maintain an approximately constant value. The resulting differences translated into discrepancies in mass flow from the range of 2.6 to 64.2 g/s, which is a more consistent result than for nozzle 1.
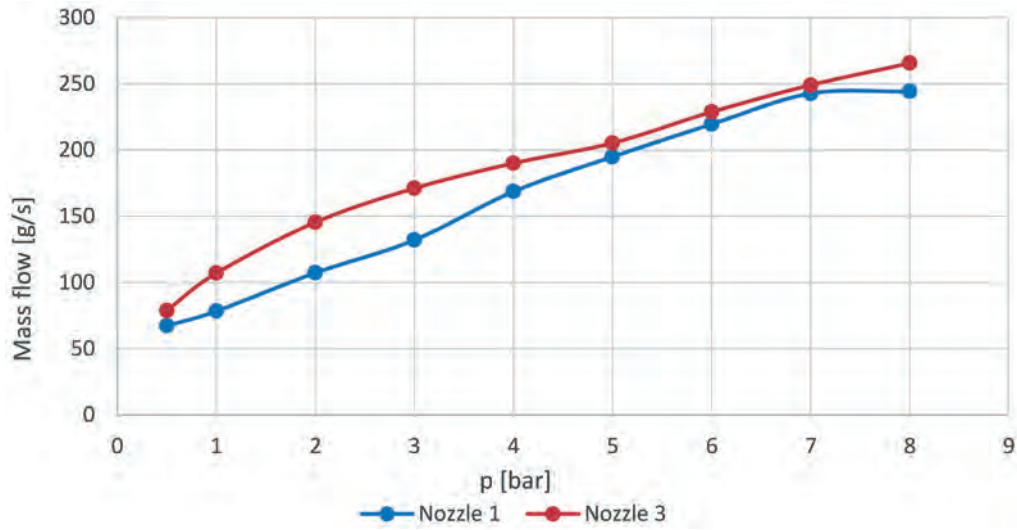
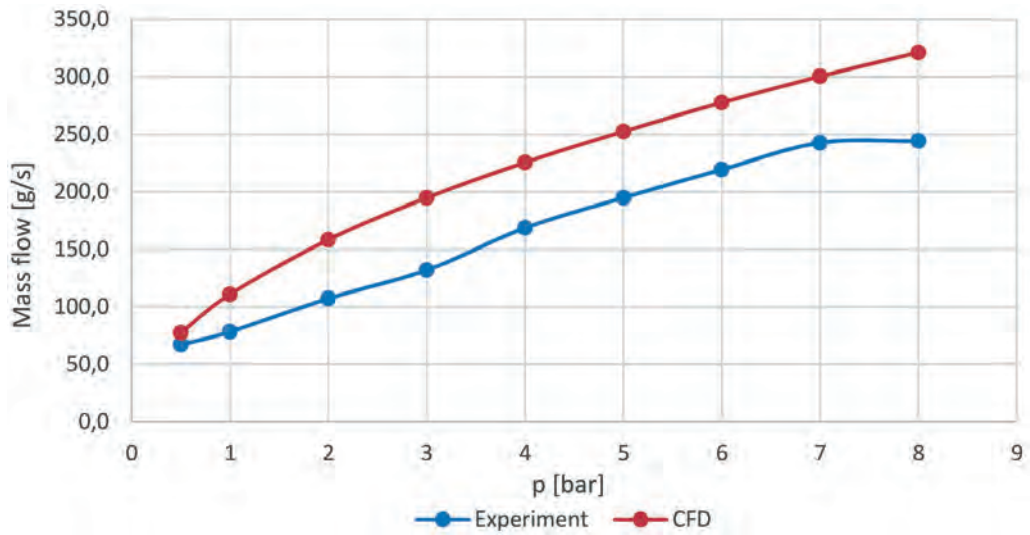*Fig. 26. Comparison of two nozzle variants. Experimental results*

Fig. 27. Comparison of experimental and CFD results for nozzle 1
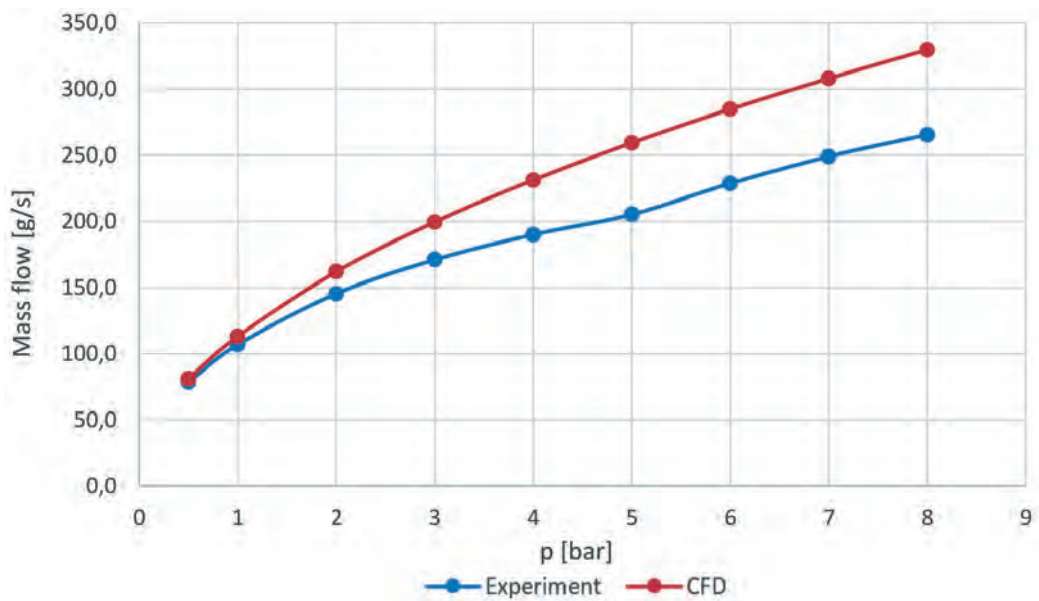

Fig. 28. Comparison of experimental and CFD results for nozzle 3

It is worth noting that the experimental results are preliminary measurements. Human factors, inaccuracy of pressure reading from the pressure gauge and numerical simplifications may have influenced the disparities found. The simulation assumed the absence of all armature and perfectly smooth walls. In reality, the current armature certainly translated into the occurrence of resistance in the flow, which may explain the lower efficiency of the nozzles in the experimental tests.

4. CONCLUSIONS

– Rapid prototyping, combined with numerical simulation, plays a key role in the design of new technologies and products.
– 3D printing can be successfully used for verification purposes for CFD models.
– The use of 3D printing saves time and costs while increasing the efficiency of the design process.
– The CFD results for the lowest pressure values, i.e. 0.5, 1 bar, are most consistent with the experiment. For nozzle 3 the relative error between analyses for these pressure values was up to 5.5%.
– Nozzle 3 in experimental and CFD analysis showed the highest efficiency.
– The maximum difference in the water flow intensity between the numerical analysis results and the experimental results was 77.1 g/s, which is a difference of almost 32.3%. Such a discrepancy occurred when analyzing nozzle 1, at a pressure of 8 bar (Fig. 26).
– DM printing for building initial prototypes of water nozzles seems to be precise enough. However, it should be kept in mind that the layered structure that is created during the printing process leads to increased flow resistance and, consequently, to higher energy losses.
– In more advanced analyses, FDM and SLA printing would need to be considered and compared to each other. It is anticipated that the use of SLA will allow for higher print resolution and lower material roughness, which should translate into greater repeatability of the results obtained.
– There is a need for further work on the issue undertaken, in particular to improve the measurement system.
– The water pump generates vibrations and pulsations that negatively affect the accuracy of pressure readings from the manometer, which certainly translates into the measurement results obtained in the experiment.

– The higher the pressure generated by the pump, the greater the vibrations it generates, which may explain the greater discrepancy in the results for higher pressure values.
– Taking into account the graduation of the pressure gauge and the vibrations that occurred during the execution of the experiment, the differences in pressure values between the CFD model and the experiment can be ±0.1 bar.
– The experimental results are only preliminary measurements. Based on the analysis, it was concluded that it is necessary to expand the measuring station to more accurately control the value of the pressure generated by the water pump.
– The modernized measuring station should include the installation of pressure transducers, inverters and a flow meter. This will allow for a more reliable assessment of the compliance of CFD simulations and a comparison of different 3D printing techniques.

Acknowledgement

References

[1] Davis R.: *What is Rapid Prototyping? Techniques, Software, Examples and Advantages – The Engineering Projects*. https://www.theengineeringprojects.com/2021/05/what-is-rapid-prototyping-techniques-software-examples-and-advantages.html [5.04.2024].
[2] Schlick J.: *What is Rapid Prototyping: Process, Stages, Types and Tools – TechniWaterjet*. https://www.techniwaterjet.com/what-is-rapid-prototyping-process-stages-types-and-tools/ [5.04.2024].
[3] Laska-Leśniewicz A.: *Wykorzystanie metod szybkiego prototypowania (rapid prototyping) w nowoczesnej medycynie*. Politechnika Łódzka, Wydział Mechaniczny Instytut Inżynierii Materiałowej, Zeszyty Naukowe Towarzystwa Doktorantów UJ 2017, 15 (2), s. 39–48.
[4] Markforged: *Understanding Rapid Prototyping with 3D Printing*. https://markforged.com/resources/blog/understanding-rapid-prototyping-with-3d-printing [7.04.2024].
[5] Larsson R., Ringertz U., Lundström D., Sobron A.: *Rapid prototyping in aircraft design using CFD, wind tunnel and flight testing*, ICAS 2022 Congress, Stockholm 2022.
[6] Takeda H., Ohtake Y., Suzuki H.: *3D printing CFD simulation results using structural mechanics*. Journal of Computational Design and Engineering 2020, 7(3): 287–293. https://doi.org/10.1093/jcde/qwaa024.
[7] Industrie-network: *Dysze wodne do Spraylab – Industrie Network*. https://www.industrie-network.com/dysze-wodne-do-spraylab/ [12.04.2024].
[8] SICK: *Nozzle regulation in a water turbine – Hydropower*. https://www.sick.com/pl/en/industries/energy/renewables/hydropower/nozzle-regulation-in-a-water-turbine/c/p675075power/nozzle-regulation-in-a-water-turbine/c/p675075 [14.05.2024].
[9] Synapo: *Dysze mgłowe – charakterystyka, zastosowanie i zasada działania*. https://synapo.pl/do-czego-sluza-dysze-mglowe/ [19.05.2024].

[10] Spraying Systems Europe: *Why spray nozzles are essential for a performant cooling process*. https://www.spray.com/en-eu/blog/why-spray-nozzles-are-essential-for-a-performant-cooling-process [21.05.2024].

[11] Lechler: *Spray Nozzles for The Energy Industry*. https://www.lechlerusa.com/en/markets/the-energy-industry [24.05.2024].

[12] Prostański D., Jedziniak M.: *Rozwój systemów zwalczania zagrożeń pyłowych*. Maszyny Górnicze 2013, 2: 87–98.

[13] Buksa D.: *Analiza numeryczna konwekcji wymuszonej nanopłynu srebra w kanale kołowym*. Akademia Górniczo-Hutnicza, Kraków 2023 [engineering thesis].

[14] Zore K., Parkhi G., Sasanapuri B., Varghese A.: *Ansys Mosaic Poly-Hexcore Mesh For High-Lift Aircraft Configuration*, 21st Annual CFD Symposium, Bangalore 2019.

[15] Wimshurst A.: *[CFD] Enhanced Wall Functions in ANSYS Fluent*. https://www.youtube.com/watch?v=h5OiFpu0L4M&ab_channel=FluidMechanics101 [12.12.2023].

[16] ANSYS FLUENT 12.0 User's Guide – 6.2.2 Mesh Quality. https://www.afs.enea.it/project/neptunius/docs/fluent/html/ug/node167.htm [12.05.2024].

[17] Jurkowski S., Janisz K.: *Analiza wpływu parametrów siatki obliczeniowej na wynik symulacji przepływomierza*. Autobusy – Technika, Eksploatacja, Systemy Transportowe 2019, 235, 12. http://ojs.inw-spatium.pl/index.php/Autobusy/article/view/997 [4.11.2022].

[18] Symkom: *ANSYS Fluent Mosaic – nowa technologia generacji siatki zawierająca elementy hexahedralne i polihedralne*. https://symkom.pl/ansys-fluent-mosaic/ [18.06.2022].

[19] Ansys Fluent Theory Guide. http://www.ansys.com [18.06.2022].

[20] Kryś M., Pawłucki M.: *CFD dla inżynierów. Praktyczne ćwiczenia na przykładzie systemu ANSYS Fluent*. Helion, Gliwice 2020.

DOMINIK BUKSA, M.Sc. Eng.
Strata Mechanics Research Institute
Polish Academy of Sciences
ul. W. Reymonta 27, 30-059 Krakow, Poland
dominik.buksa@imgpan.pl

PAWEŁ MADEJSKI, Prof.
MICHAŁ KARCH, Ph.D., Eng.
Faculty of Mechanical Engineering and Robotics
AGH University of Krakow
al. A. Mickiewicza 30, 30-059 Krakow, Poland
{madejski, karch}@agh.edu.pl